Lab on a Chip

PAPER

View Article Online
View Journal | View Issue

Cite this: *Lab Chip*, 2023, **23**, 4565

Ultra-thin and ultra-porous nanofiber networks as a basement-membrane mimic†

Philip M. Graybill, ‡[a] Edward J. Jacobs IV, ‡[a] Aniket Jana,[b] Atharva Agashe,[b] Amrinder S. Nain*[b] and Rafael V. Davalos *[a]

Received 7th April 2023,
Accepted 17th September 2023

DOI: 10.1039/d3lc00304c

rsc.li/loc

Current basement membrane (BM) mimics used for modeling endothelial and epithelial barriers *in vitro* do not faithfully recapitulate key *in vivo* physiological properties such as BM thickness, porosity, stiffness, and fibrous composition. Here, we use networks of precisely arranged nanofibers to form ultra-thin (~3 μm thick) and ultra-porous (~90%) BM mimics for blood–brain barrier modeling. We show that these nanofiber networks enable close contact between endothelial monolayers and pericytes across the membrane, which are known to regulate barrier tightness. Cytoskeletal staining and transendothelial electrical resistance (TEER) measurements reveal barrier formation on nanofiber membranes integrated within microfluidic devices and transwell inserts. Further, significantly higher TEER values indicate a biological benefit for co-cultures formed on the ultra-thin nanofiber membranes. Our BM mimic overcomes critical technological challenges in forming co-cultures that are in proximity and facilitate cell–cell contact, while still being constrained to their respective sides. We anticipate that our nanofiber networks will find applications in drug discovery, cell migration, and barrier dysfunction studies.

Introduction

Physiological barriers are found throughout the body, and their integrity is paramount for maintaining healthy functionality.[1] Important physiological barriers include the alveolar–capillary barrier,[2,3] intestinal–mucosal barrier,[4] dermal barrier,[5] renal–epithelial barrier,[6] and the blood–brain barrier (BBB).[7–13] Barrier properties are derived from junctional complexes that regulate transport between cells (paracellular transport) and from specialized transporter proteins that regulate transport across the cell membrane (transcellular transport).[11] Barrier dysfunction has been implicated in many serious conditions, such as Alzheimer's disease,[14] pulmonary edema,[15] chronic kidney disease,[16] and atopic dermatitis.[17] Physiological barriers also present significant blockades for therapeutic agents. Limited drug permeability across these barriers renders many promising therapies ineffective, with nearly 100% of large drugs and 98% of small drugs unable to penetrate the BBB.[18] Barrier properties are also key for immune cell trafficking, cancer metastasis, and nanoparticle transport.[19]

Although barrier properties are maintained by endothelial and epithelial monolayers, a key component is the basement membrane (BM).[20] The BM is a thin layer (about 50–300 nm) of extracellular matrix (ECM), composed of collagen, fibronectin, and laminin,[20,21] that provides support for endothelial and epithelial cells, while also separating these cells from supporting cells. Endothelial and epithelial cells are regulated by cell–cell crosstalk from the supporting cells across the BM. The specialized brain vascular endothelial cells gain their unique transport-restricting properties when in close contact with adjacent cell types across the BM (Fig. 1a). *In vivo* and *in vitro* studies have shown pericytes and astrocytes regulate endothelial barrier function. Brain endothelial cells make direct contact with pericytes through peg-and-socket connections (Fig. 1a).[22] Astrocyte endfeet surround capillaries in the brain and regulate endothelial behavior through the release of soluble factors such as VEGF, TGFβ, GDNF, and bFGF.[23–25]

Many *in vitro* models have been developed for investigating barrier properties.[26] These models rely on endothelial or epithelial monolayers cultured on BM constructs, designed to mimic the *in vivo* BM. Although numerous BM mimicking materials have been developed, to date these membranes still have significant limitations.[27] Table 1 summarizes the advantages and disadvantages of several engineered BMs. The most widely used *in vitro* BM mimics are track-etched

[a] *Bioelectromechanical Systems Lab, Department of Biomedical Engineering and Mechanics, Virginia Tech, Blacksburg, VA, USA. E-mail: davalos@vt.edu*
[b] *Spinneret-Based Tunable Engineering Parameters (STEP) Lab, Department of Mechanical Engineering, Virginia Tech, Blacksburg, VA, USA. E-mail: nain@vt.edu*
† Electronic supplementary information (ESI) available. See DOI: https://doi.org/10.1039/d3lc00304c
‡ These authors contributed equally.

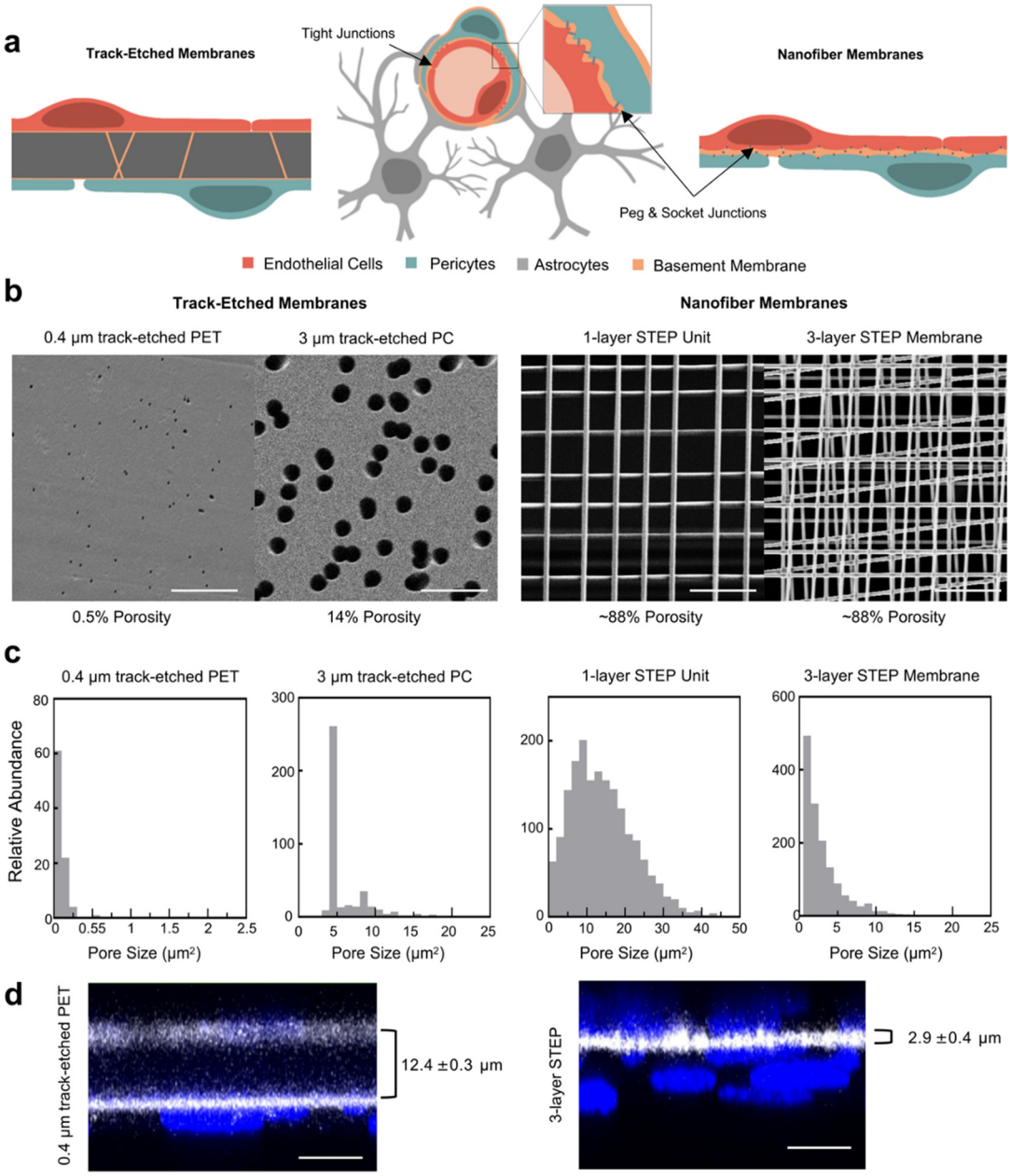

Fig. 1 Ultra-thin, ultra-porous nanofiber networks offer significantly improved physical properties compared to track-etched membranes. a) Schematic representations of track-etched (left) *vs.* STEP nanofiber membranes (right) as models of the blood–brain barrier *in vivo* (middle). b) SEM images reveal the pore structure of i) 0.4 μm diameter track-etched PET membranes, ii) 3 μm diameter track-etched PC membranes, iii) 1-layer crosshatch STEP unit, and iv) 3-layer STEP nanofiber membranes. The 1-layer crosshatch STEP unit was formed with 600 nm diameter fibers spaced ~4 μm apart within each layer, and the 3-layer STEP membrane is comprised of 3 crosshatch units spun on top each other and bonded. Track-etched membranes have randomly located pores of uniform size whereas the nanofiber membranes have precisely-organized pore structures with a greater distribution of pore sizes. c) Pore size distributions show nanofiber membranes have a wider pore size distribution than track-etched membranes. The 3-layer membranes have an average pore size significantly lower than the 3-μm diameter track-etched membrane. The pore size, thickness, and porosity of the nanofiber membranes can be controlled by fiber spacing, diameter, and the number of STEP units. d) The nanofiber membranes are significantly thinner than conventional track-etched membranes ($p < 0.001$). Conventional PET membranes are 10–12 μm thick (left) whereas 3-layer nanofiber membranes are approximately 3 μm thick (right). Rhodamine fibronectin (white) indicates membrane surfaces and blue indicates DAPI. Scale bars 10 μm.

polycarbonate (PC), polyester or polyethylene terephthalate (PET), and polytetrafluoroethylene (PTFE).[28–39] These semi-permeable membranes are commercially available with cylindrical pores of 0.4, 1, 3, 5, or 8 μm-diameter.

For barrier models, endothelial cells are cultured on one side of the membrane, and unless migration is desired, small pore sizes (typically 0.4 or 1 μm) are used.[34,38] These membranes, however, have limited physiological relevance in

Table 1 Membrane-mimics used for *in vitro* modeling

Membrane types	Desirable properties	Undesirable properties	Ref.
Track-etched PC, PET, PTFE	Commercially available (0.4, 1, 3, 8 μm pores) Transparent (PET, PTFE) Biocompatible	Non-fibrous Thick (~10–12 μm) Low porosity (~0.5–15%) Translucent (PC) Stiffer than *in vivo*	38, 28–39
Silicon nitride	Ultra-thin (50 nm –1 μm) to facilitate cell–cell contact High porosity (approaching 50%) Structured pore geometry and size (~400 nm square pores) Transparent	Non-fibrous Poor cell adhesion to SiN Requires nanofabrication Stiffer than *in vivo*	40–42
Collagen or vitrified collagen	Fibrous Native ECM	Pore size determined by fabrication Low porosity due to small pores Thick (>10 μm)	43–48
Patterned PDMS/Mylar	Transparent Flexible (PDMS) Can be highly porous	Generally thick (5 μm) Non-fibrous Fragile Requires nanofabrication	2, 49–53
Electrospun nanofibers	Fibrous Variable pore sizes Relatively high porosity Can be bioactive Can have good mechanical strength	Relatively thick (>4 μm) Random arrangement of pores Wide pore size distribution Not transparent	54–57
STEP nanofibers	Ultra-thin (<3 μm) Ultra-porous (~90%) Transparent Fibrous No nanofabrication or cleanroom Excellent biocompatibility	Mildly distributed pore sizes Mildly fragile	This work

PC, polycarbonate; PET, polyethylene terephthalate; PTFE, polytetrafluoroethylene.

key aspects. Firstly, these membranes are generally 10–12 μm thick (or 30 μm for PTFE), over 100 times thicker than the BM *in vivo*. This inhibits direct cell–cell contact across the membrane and limits the transport of soluble factors between adjacent cell types. Secondly, these membranes have inherently low porosity; track-etch membranes typically have maximum porosities of around 15% for 1 μm pores. Conventional track-etched membranes have porosities as low as 0.5% which can also obscure transendothelial electrical resistance (TEER) measurements.[58] Finally, the flat, sheet-like construction of these membranes cannot mimic the fibrous nature of the BM for physiological relevance.[48] Besides limited physiological relevance, track-etched membranes can obscure brightfield imaging (PC is translucent) and confocal imaging due to the thickness of the membrane.

Several BMs are under development as alternatives to track-etched membranes, including nanofabricated SiN membranes,[40–42] electrospun nanofibers,[54–56] patterned materials such as PDMS and mylar,[49–52] and native ECM membranes such as collagen and collagen vitrigel membranes.[43–48] Nanofabricated SiN membranes can be extremely thin (50 nm to 1 μm), have evenly distributed pores, and are optically transparent.[40–42] However, these membranes require expensive microfabrication processes, are non-fibrous, and the SiN poses cell attachment problems.[40] Similarly, non-fibrous photolithographically-patterned Mylar[50] and PDMS[2,49,51] membranes have been fabricated with relatively high porosity (up to ~50%), controlled pore size/location, moderate thickness (generally 5–50 μm) and are optically transparent. Thinner PDMS membranes have been fabricated at 2 μm, at the cost of low porosity (2%).[53] To achieve fibrous membranes, electrospinning techniques have been used.[54–56] These membranes have disadvantages such as large thicknesses (>10 μm) and randomly distributed fibers and pores. Native extracellular matrix (ECM) membranes have also been developed,[43,48,59] such as vitrified collagen membranes,[44–47] but these membranes have low porosity due to the vitrification process and are rather thick (≥10 μm).

We introduce ultra-thin, ultra-porous fibrous networks fabricated with the non-electrospinning Spinneret-based Tunable Engineered Parameters (STEP) method.[60,61] Our BM mimicking STEP nanofiber networks offer several advantages compared to other membranes. Firstly, STEP membranes are ultra-thin and can be fabricated close to physiologically relevant thicknesses. Secondly, STEP membranes achieved porosities over 80%. Because our STEP membranes are thin and highly porous, significant crosstalk and physical contact can be achieved between cells cultured on adjacent sides of the membrane. Thirdly, STEP membranes are fibrous, like the native BM, and more relevant than commercial membranes. Lastly, STEP membranes are made of polystyrene, making them highly biocompatible and excellent for cell adhesion. They can be coated with ECM-like proteins to create a natural surface for cell growth. We demonstrate the physiological utility of our nanofiber membranes by modeling the BBB using primary human endothelial cells and pericytes in monoculture and contact co-culture models within both

microfluidic and transwell devices. The two cell types can reach and make contact within the membrane, and TEER measurements robustly show the marked improvement over standard approaches. The STEP method may provide a more physiologically relevant BM than alternative membrane fabrication methods, leading to improved membranes for a vast range of applications.

Materials and methods

Nanofiber fabrication

Dense nanofiber membranes were fabricated according to the previously published STEP method.[60,61] Nanofibers were spun around scaffold supports that were laser-cut from plastic coverslips (Fisher Scientific, 0.22 mm thick) to contain a hollow region 2 mm in diameter. Liquid prepolymer was dispensed from a microneedle and nanofibers were spun around a rotating and translating scaffold substrate. The scaffold was then re-oriented 90° and spun again to create the crosshatch unit. The 600 nm-diameter fibers were prepared using a 7 wt% solution of polystyrene (MW: 2 000 000 g mol^{-1}; category no. 829; Scientific Polymer Products, Ontario, NY, USA) in *p*-xylene (X5-500; Thermo Fisher Scientific, Waltham, MA, USA). To decrease pore sizes, multiple nanofiber layers were spun across the scaffold in succession. Nanofibers were then chemically fused together. To improve the throughput of the spinning process, and to eliminate the need to remove unwanted fibers from one side of the scaffold, we secured two scaffolds back-to-back by epoxying their stubs together. Prior to integrating them into the devices, the scaffold stub was carefully cutoff, and the two scaffolds were separated from each other.

Microfluidic fabrication

Microfluidic devices were fabricated from two polydimethylsiloxane (Dow Corning, PDMS) layers that enclosed the plastic nanofiber scaffold. PDMS was mixed 10 : 1 base to cross-linker and was cured in acrylic molds at 50 °C for 4 hours. Acrylic molds were assembled from laser cut and solvent bonded layers. The lower microfluidic channel and the indentation for the nanofiber scaffold were patterned using a top and bottom acrylic mold pressed together by binder clips. Access holes for the inlet and outlets of the lower channel were punched in the lower PDMS membrane using a 1.5 mm-diameter biopsy punch, and the PDMS layer was plasma bonded (Harrick Plasma) to a glass slide. The upper microfluidic channel was similarly formed in an acrylic mold, and once cured, inlet and outlet ports were punched in the upper layer using a 1 mm-diameter biopsy punch. Finally, a top well layer was cured in an acrylic mold and 6 mm diameter holes were punched with a biopsy punch. Upper and lower microfluidic channels were 0.22 mm high, 3 mm wide, and 18 mm long. Liquid PDMS glue (10 : 1 base to cross-linker) was used to bond the nanofiber scaffold between the upper and lower channel layers. Liquid PDMS was spun at 3000 RPM for 1 minute on a glass slide and de-gassed upper PDMS layers were placed channel-side down on the PDMS layer to absorb the PDMS. Liquid PDMS was loaded into a 1 ml syringe connected to a dispensing needle. A small amount was spread on the lower PDMS layer where the indentation for the scaffold was located. The nanofiber scaffold stub was then carefully cut-off, and the scaffold was placed fiber-side down on the lower PDMS layer. The plastic scaffold containing the nanofiber network (or PET membrane for comparison) was then placed in the circular indentation and adhered in place with liquid PDMS glue.

Track-etched membranes

To enable a comparison between the nanofiber membranes, track-etched PET or PC membranes were also incorporated into the microfluidic device. PET membranes were removed from 6-transwell plates (Corning, #3450) and according to the manufacturer were 10 μm thick and had 0.4 μm diameter pores at 4×10^6 pores per cm^2. PC membranes (Millipore Sigma, TSTP02500) were also tested and according to the manufacturer were 22 μm thick and had 3.0 μm pores with a porosity of 11.3%. Both PET and PC membranes were carefully cut into ~4 × 4 mm squares and bonded to the laser-cut nanofiber scaffolds using liquid PDMS glue. Liquid PDMS was spun at 3000 RPM on a glass slide. One side of the plastic scaffold was placed in contact with the glue, and then removed. The PET or PC membrane was carefully placed across the 2 mm hollow region, and then cured at 55 °C for 2 hours.

Cell culture

Human endothelial cells and pericytes were used to model the BBB. Cell culture was performed according to supplier protocols. Human cerebral microvascular endothelial cells (hCMEC/D3, EMD Millipore) were maintained in EngoGrow™-MV Complete media supplemented with 1 ng ml^{-1} FGF-2 (MilliporeSigma), and 1% penicillin/streptomycin (Life Sciences). Primary human brain microvascular endothelial cells (HBMECs, Cell Systems) were cultured in cell systems medium supplemented with 5 ml CultureBoost™. Primary human brain vascular pericytes (HBVP, ScienCell) were cultured in pericyte basal medium supplemented with 10 ml of fetal bovine serum, 5 ml of pericyte growth supplement, and 5 ml of penicillin/streptomycin solution. Cells were incubated at 37 °C and 5% CO_2.

Fluorescence microscopy and cell staining

Antibody staining was performed to investigate cell morphology. Cells were fixed and stained within the microfluidic devices. Cells were fixed in 4% paraformaldehyde for 15 minutes, washed with phosphate buffered saline (PBS), and permeabilized in 0.1% Triton-X-100 in PBS for 15 minutes. Cells were then washed with PBS and blocked with 5% normal goat serum in PBS for 15 minutes. Cells were incubated with primary antibodies mixed in antibody dilution buffer consisting of PBS

supplemented with 1 : 100 w/v bovine serum albumen (BSA) and 1 : 333 v/v Triton X-100. Endothelial cells were stained for ZO-1(ZO-1 polyclonal antibody, Invitrogen # 40-2200, 1 : 100) and VE-cadherin (CD144 (VE-cadherin) monoclonal antibody (16B1), eBioscience, #14-1449-82, 1 : 100). Pericytes were stained for calponin (Abcam, recombinant anti-calponin 1 antibody [EP798Y] (ab46794), 1 : 200). Cells were incubated with primary antibodies overnight at 4 °C. Cells were washed with PBS, and secondary antibodies (Alexa Flour 488, 555, or 647 at 1:400 in antibody dilution buffer) were added to the device for 45 minutes in the dark at room temperature. Finally, cells were washed with PBS, incubated with 300 nM DAPI in PBS for 10 minutes, and then flushed with PBS for imaging.

Imaging was performed with a 63× water immersion objective (1.15 NA) in a Zeiss LSM 880 confocal microscope. *Z*-Stacks were taken with step sizes 0.36 μm to 0.5 μm for STEP nanofiber and PET membranes, respectively. Optimal laser scanning settings were utilized for image acquisition.

Since >88% of our nanofiber membranes is free space, we observed that cell bodies and nuclei from both co-culture layers frequently settled into the free space within the nanofiber membrane. To calculate the effective distance between the two co-cultured layers, we imported the Z-stack images into ImageJ. There were clear borders for the cell membrane of both the pericytes and endothelial cells (see Movies S1–S4†). We chose 20 random points across the region imaged (N = 4 devices, n = 80 for both PET and STEP nanofiber membranes) and measured the distance in the *z*-direction between the stained cell membranes across the nanofiber or PET membrane. The distance between nuclei was calculated as the *z*-distance between the two nearest nuclei (N = 4 devices, n = 20 for both PET and STEP nanofiber membranes).

Diffusion experiments

Diffusion experiments were performed by adding McCormick culinary blue food color dye (mixture of blue 1 (MW: 792.85 Da) and red 40 (496.42 Da)). To prevent dye flow across the membrane, packing tape was used to seal the inlet and outlet ports of the upper channel while filling the device through the lower channel. To decrease evaporation from the device, the top of the device was then sealed with packing tape. Images were collected every minute for 10 hours at room temperature. Diffusion data were then analyzed in ImageJ to determine the time constants of diffusion.

Experimental methods

To prepare the microfluidic devices for experiments, vacuum-degassed devices were sterilized with ethanol and then washed with PBS. The devices were incubated overnight at 37 °C with 4 μg ml^{-1} of human fibronectin in PBS. For imaging experiments, rhodamine-conjugated fibronectin (Cytoskeleton Inc) was used at the same concentration. The following day, devices were flushed with endothelial media and incubated for another hour at 37 °C. Endothelial cells were passaged according to supplier instruction and suspended at 1 × 10^7 cells per ml (2200 cells per mm^2) for the hCMEC/D3 cells or at 5 × 10^6 cells per ml (1100 cells per mm^2) for the HBMECs cells in cell culture media. Before pipetting the cells into the lower channel of the device, the inlet and outlet of the upper channel were blocked with PDMS-clogged pipet tips to prevent fluid flow across the membrane. Cells were then added to the lower channel and the devices were immediately inverted and incubated at 37 °C for three hours. The devices were then place right-side up, the pipet tips removed, and additional media was added to the device wells. Devices were incubated overnight to allow endothelial monolayer formation. The following day, pericytes were passaged according to supplier instructions and resuspended in pericyte media at 5 × 10^6 cells per ml (1100 cells per mm^2). PDMS-clogged pipet tips were used to block the lower channel inlet and outlets, and the cell suspension was added to the upper channel. After incubation for three hours, the pipet tips were removed, and additional media was added. Pericytes were allowed to spread and interact with the endothelial cells for 24 hours, after which time the device was fixed with 4% paraformaldehyde for imaging.

Transwell experiments

To explore tight junction integrity for both mono- and co-culture models, we incorporated our custom scaffolds into a 24-well transwell system. The same scaffolds and membranes for the microfluidic devices were used, as the scaffolds are the same diameter as the bottom of a 24-well plate transwell insert (CellTreat, #230635). The manufactured membranes on the bottom of the transwell inserts were removed and liquid PDMS was used to bond our custom scaffolds in place, with the membrane facing the bottom of the insert. The transwells were sterilized with ethanol and UV light. 4 μg ml^{-1} of human fibronectin was added to the transwell and incubated over night at 37 °C. Warm media was added, and initial TEER values were taken to measure the membrane resistances. TEER values were obtained using the EVOM3 epithelial TEER meter with stick electrodes (World Precision Instruments). The values were obtained at 12.5 Hz with a 10 μA applied current. The transwells were then removed and inverted. Endothelial cells and pericytes were passaged and seeded at the same concentration as with the microfluidic devices. The endothelial cells were added and allowed to attach for two hours at 37 °C. The transwells were then placed into the 24-well plate with the media. HBMEC attachment was verified with a light microscope. The transwell devices were allowed to incubate overnight. HBVPs were added to the inside of the transwell the following day. TEER measurements for day 1 were taken prior to adding HBVPs. TEER measurements were then taken every day for 5 days, directly after removing from the incubator to maintain the temperature at 37 °C. Barrier formation was verified on day 2 with 4 μM calcein-AM live-dead stain added directly to the transwell.

Porosity, pore size and nominal thickness calculations

Pore size distributions for the nanofiber membranes and track-etched membranes were determined by thresholding Scanning Electron Microscope (SEM) images of the membranes using ImageJ's particle analysis menu. Porosity values were estimated based on fiber diameters and fiber spacing. Porosity can be calculated as:

$$\text{Porosity} = \frac{V_S}{V_M} \cong \frac{V_M - V_F}{V_M}$$

where V_M is the total volume of the membrane, V_F is the total volume of the fibers, and V_S is the volume of free, accessible space within the membrane. V_F depend linearly on the number of fibers within a layer. The number of layers does not affect porosity for thin membranes with a low number of layers since it can be assumed that every point within the membrane is accessible from any other point.[62] Therefore, porosity is determined by the fiber diameter and fiber spacing. The porosity of our 1-layer and 3-layer membranes were estimated using nominal 600 nm diameter fibers and 4 μm spacing.

Nominal thicknesses of the nanofiber and PET membranes were calculated using SEM images as the thickness from the topmost point of the membrane to the bottom most point of the membrane.

Statistical analysis

All data are presented as mean ± STD. Statistical analysis was performed in Graphpad Prism 9.4.0 (GraphPad Software, San Diego, California USA). Student *t*-tests were performed to determine the significance of membrane thickness. One-way ANOVA with *post hoc* tests were performed to find the significance between data sets for porosity, diffusion, and TEER measurements. The significance level was $\alpha = 0.05$.

Results

Ultra-thin, ultra-porous nanofiber membranes are fabricated by the STEP method

To replicate the ultra-thin and ultra-porous properties of the *in vivo* BM, we used the STEP method[60,61] to deposit dense networks of biocompatible polystyrene nanofibers with controlled fiber diameters (100 nm–10 μm) and controlled fiber spacing (as low as 3 μm).[63] Suspended crosshatch nanofiber patterns were fabricated by stacking orthogonal fiber layers on top of previously deposited fibrous layers to form one crosshatch unit (Fig. 1b). One crosshatch unit has too large of pores to constrain cell monolayers to their respective sides, so multiple crosshatch units can be spun on top of each other at an angle (0–90°) to form thicker but more confining membranes. The nanofibers were then chemically fused together to improve the integrity of the membrane. We demonstrate the depositional control for the 3-layer step membrane and quantify the fiber orientation for the two orthogonal arrays (Fig. S2†). Through the STEP process, fiber orientations were tightly controlled in both arrays with a standard deviation <0.25° between the intended and actual deposition angle.

STEP nanofiber membranes were compared against the conventional barrier-modeling PET membranes with 0.4 μm pore sizes with an extremely low porosity of less than 0.5% and 3 μm diameter pore PC membranes with a porosity of ~15% (Fig. 1b). The STEP nanofiber membranes have extremely high porosities for two nanofiber membrane configurations investigated: 1- and 3-layers of crosshatch unit membranes with 600 nm fiber diameters (586 ± 58.9 nm; range 503–703 nm). For both the 1-layer and 3-layer membranes, we found the theoretical porosity to be ~88%. This represents a 220× increase over the 0.4 μm pore PET membranes and a 6.5× increase over the 3 μm PC membranes. Further, analysis of the *Z*-projected (2D) from SEM images reveals the average pore size is 14.0 ± 8.2 μm^2 for the 1-layer membrane and 2.5 ± 2.5 μm^2 for the 3-layer membrane (Fig. 1c). One single crosshatch layer has roughly equivalent pore sizes as a 5 μm diameter track-etched membrane (pore size ~19.6 μm^2), and our 3-layer nanofiber membranes have pore sizes roughly between 1 μm and 3 μm diameter track-etched pores (pore sizes 0.8 μm^2 and 7.1 μm^2, respectively). Our 3-layer STEP membrane has a significantly smaller pore size than 3 μm diameter PC membrane ($t = 22.4$, $p < 0.0001$).

In addition to the ultra-high porosities of our nanofiber membranes, our membranes are also significantly thinner than conventional membranes. Conventional track-etched PET and PC membranes range from 10 to 12 μm in thickness, over 100× the thickness of the BM *in vivo*. Our nanofiber networks offer at least a 3-fold decrease in thickness (Fig. 1d). Our 1-layer membranes are nominally 1.0 μm thick, while our 3-layer membranes are nominally 2.9 μm thick. At ≤3 μm nominal thickness and highly porosity, our membranes can enable significant cell–cell interactions across the membrane, by allowing easier transmembrane diffusion and co-cultures to reach into the membrane without crossing over. Overall, we demonstrate a significant advancement in fabrication of BM mimics through precise patterning of suspended fiber networks in multiple layers. These properties are summarized in Table 2.

Nanofiber membranes enhance trans-membrane diffusion

Next, we inquired if the combination of high porosity and low thickness of our nanofiber membranes would enable enhanced molecular diffusion across the membrane and support the marked increase in theoretical porosity. To visually demonstrate increases in transmembrane diffusion, we performed time-lapse diffusion experiments by incorporating the nanofibers in a microfluidic device (Fig. 2). To create our microfluidic model, we fabricated two patterned PDMS channel layers that enclosed the scaffold with a

Table 2 Thickness, porosity, and average pore sizes and distribution for nanofiber and track-etched membranes

Membrane type	Structure	Thickness	Calculated 3D porosity	Pore size (μm^2)	
				Median	Mean ± STD
1-Layer STEP	600 nm nanofibers	≤1.2 μm	88%	12.98	14.03 ± 8.18
3-Layer STEP	600 nm nanofibers	≤3.0 μm	88%	1.62	2.45 ± 2.55
Track-etched PC	3.0 μm cylindrical pores	22 μm[a]	11.3%[a]	4.54	6.07 ± 3.24
Track-etched PET	0.4 μm cylindrical pores	12 μm 10 μm[a]	0.5%[a]	0.09	0.11 ± 0.06

[a] According to manufacturer information.

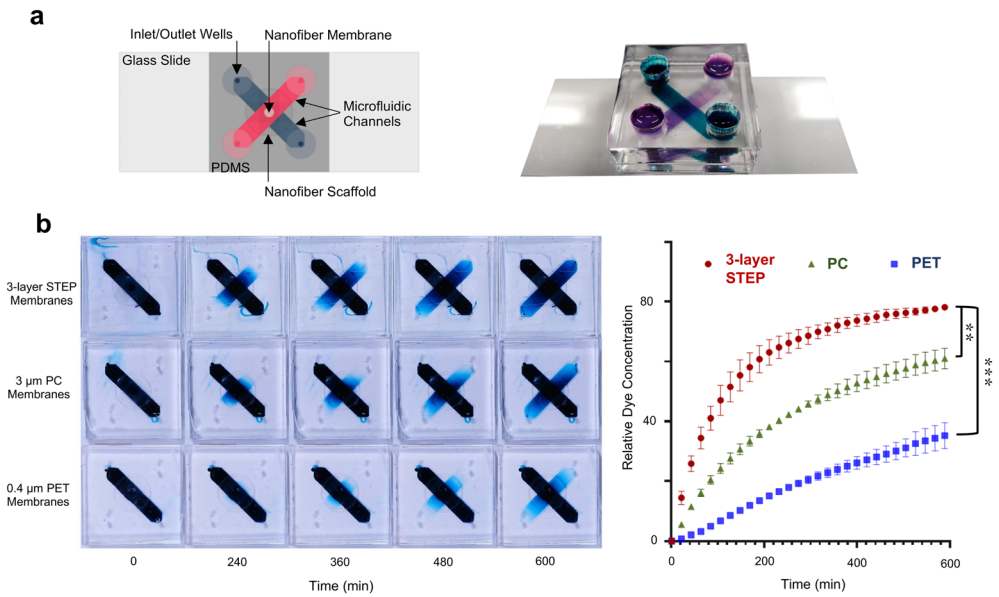

Fig. 2 STEP nanofiber membranes enhance trans-membrane diffusion compared to track-etched membranes. a) A three-layer PDMS microfluidic BBB chip contains two orthogonal channels separated by a dense nanofiber network that replicates the basement membrane for co-culture BBB models. b) Diffusion of food dye from the lower channel to the upper channel shows that 3-layer nanofiber membranes enable enhanced diffusion compared with PC and PET membranes. Amount of dye concentration is quantified by color intensity and normalized relative to the bottom channel. STEP membranes have significantly higher rates of diffusion transmembrane compared to PET (p-value < 0.001) and PC (p-value < 0.01) track-etched membranes.

nanofiber membrane at the intersection, so diffusion from one channel to another could only occur by passing through the membrane. For comparison studies, conventional track-etched PET or PC membranes were bonded to identical laser-cut scaffolds. Food dye was injected into the bottom channel and imaged every minute for 10 hours (Fig. 2b). The 3-layer nanofiber membrane had a significantly increased rate of dye diffusion. The time constants of diffusion were calculated to be 72.3 ± 10.3 min, 199 ± 11.5 min, and 574 ± 45 min for the 3-layer nanofiber, 3 μm PC, and 0.4 μm PET membranes, respectively. Despite the 3-layer nanofiber membrane having a significantly smaller pore size compared to the PC membrane, it has a 3× higher rate of diffusion, supporting the higher calculated theoretical porosity.

Nanofiber membranes support endothelial monolayer formation

Given the improved physical properties of our nanofiber membranes compared to track-etched alternatives, we investigated whether they could be used to recapitulate critical BBB physiology *in vitro*. We found that two human brain microvascular cell lines were able to form intact monolayers on the 3-layer nanofiber membrane: immortalized human cerebral microvascular endothelial cells (hCMEC/D3) and primary human brain microvascular endothelial cells (HBMECs). Endothelial cells were seeded at high densities on the fibers, and monolayers began forming within 24 hours. Complete monolayers of HBMECS and hCMEC/D3s formed after 72 hours of culture on the fibers (Fig. 3). Further, confocal microscopy reveals that endothelial cells were confined to one side of the membrane (Movie S1†). Nanofiber networks were stained with rhodamine-conjugated fibronectin.

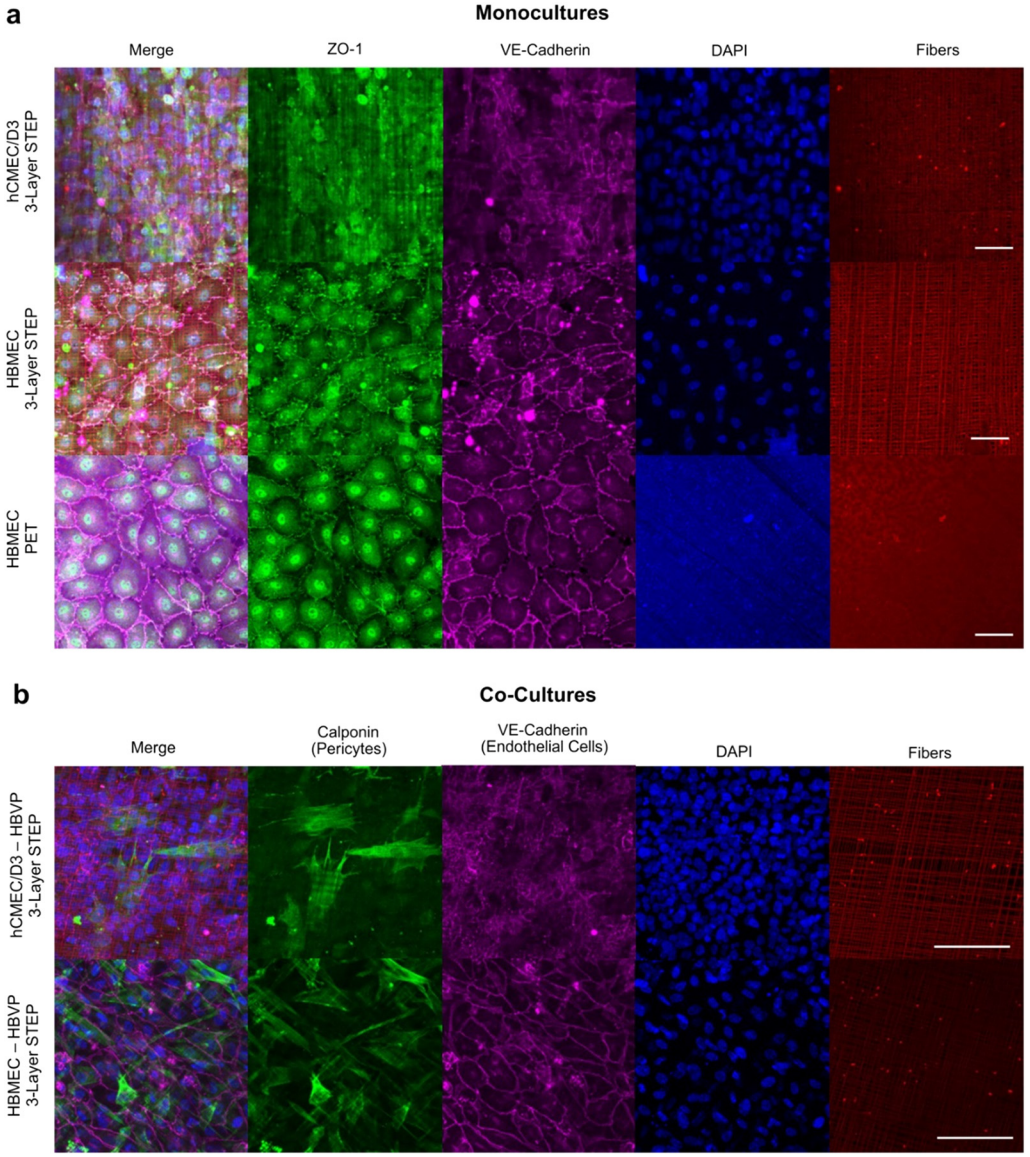

Fig. 3 Endothelial cells form complete monolayers on nanofiber scaffolds and can be co-cultured with pericytes. a) Immortalized endothelial cells (hCMEC/D3s, top row) and primary human brain microvascular endothelial cells (HBMECs) cultured in monolayer on nanofibers (middle row) and PET membranes (bottom row). Expression of ZO-1 (green), VE-cadherin (magenta), DAPI (blue), and rhodamine-conjugated fibronectin (red) are shown. b) hCMEC/D3s (top row) stained with VE-cadherin and primary pericytes (HBVPs) stained for calponin demonstrate successful co-culture across the nanofiber membrane. HBMECs (bottom row) likewise show characteristics of monolayer formation along with pericyte localization. Scale bars are 20 μm.

To explore the integrity of the monolayers, we interrogated the expression of tight junction markers ZO-1 and VE-cadherin for both monolayer cultures of HBMECs and hCMECS/D3s. Both endothelial cell lines had a significant expression of ZO-1 and localization of VE-cadherin (Fig. 3a), showing both tight junction expression and monolayer formation. The 3-layer nanofiber membranes and 0.4 μm PET membranes both showed ubiquitous ZO-1 and VE-cadherin expression for HBMECs with well-defined boundaries between cells.

Nanofiber co-cultures of endothelial cells with pericytes enable cell–cell interactions across the barrier

Due to the low thickness and high porosity of our membranes, we next sought to explore the utility of the STEP nanofiber membrane to form a physiologically relevant co-culture model. We cultured human brain vascular pericytes (HBVPs) and endothelial cells on opposite sides of the nanofiber membrane to mimic the spatial configuration of these cells *in vivo*. As shown in Fig. 3b, pericytes were successfully cultured opposite endothelial monolayers for both hCMEC/D3 and HBMEC cells.

We used rhodamine fibronectin (white) to promote cell adhesion and visualize the membranes, and cell nuclei are stained with DAPI (blue). For the track-etched membranes, there are two distinct lines of rhodamine fibronectin expression on the top and bottom of the membrane, with the bottom being noticeably more visible. The track-etched membranes are not optically transparent, which can lead to

loss of image resolution. Further, they are auto-fluorescent and emit blue light when excited (Fig. 3a). This may impede imaging with a similar excitation wavelength. The nanofiber membranes, however, do not share either disadvantage. We did not observe a visible separation of rhodamine expression across the 3-layer STEP membrane and found minimal loss of image resolution through the STEP membranes, indicated by the increase in resolution for cells on top of the membrane.

Unlike conventional tracked-etched membranes which are flat, the fibrous nature of our nanofiber membrane allows for a 3D environment for cell attachment.[63,64] The interface between the monolayers and the track-etched membrane is clearly visible in the confocal *Z*-stack image.

While the nominal thickness of the nanofiber membranes was calculated to be 2.9 ± 0.4 μm, the effective thickness is smaller due to cells settling and occupying space within the nanofiber membrane. We observed that the nuclei (DAPI) for both pericytes and endothelial cells are within the free space of the nanofiber membrane (Fig. 4a). The average separation between nuclei across the membrane was 1.75 ± 0.60 μm, with separations ranging from 0.75–3 μm (Fig. 4c). Importantly, we observed no instances of nuclei from one cell layer crossing over to the other side.

Further, we observed that the cytoplasmic membranes of these cells penetrated deeper within the STEP membranes, with many instances where there is no observable separation between the endothelial and pericyte plasma membranes. We calculated the effective distance between the two co-culture layers and found an average separation of 0.69 ± 0.47 μm with a range of 0–1.8 μm. The separation between the two co-cultured layers is significantly less (p-value < 0.0001) than the separation between the nuclei. This supports the observations that the nuclei are confined to their respective sides, but the cells are allowed to reach into the free space to come into contact. From confocal images, we calculated the average nucleus diameter to be 12.4 ± 1.5 ($n = 40$; range 10.1–16.7 μm). Migration studies frequently employ membranes with pore diameters >3 μm,[65] so it isn't surprising that cells can partially enter the porous STEP membrane, without crossing over. The calculated separation between nuclei and co-culture layers for the PET membrane was 11.5 ± 0.40 μm and 11.4 ± 0.57 μm, respectively. There was not a significant difference between the nuclei and membrane separation for the PET membrane.

Further, multiple experiments were observed demonstrating the close proximity of the co-cultures on the STEP nanofiber membrane and the ability of cells to come into contact within the membrane (Fig. S1c and Movies S2–S4†), with no visible separation between the two cell monolayers. Movies S2 and S3† show that HBMEC monolayers are confined to the bottom of the membrane, with pericyte processes reaching

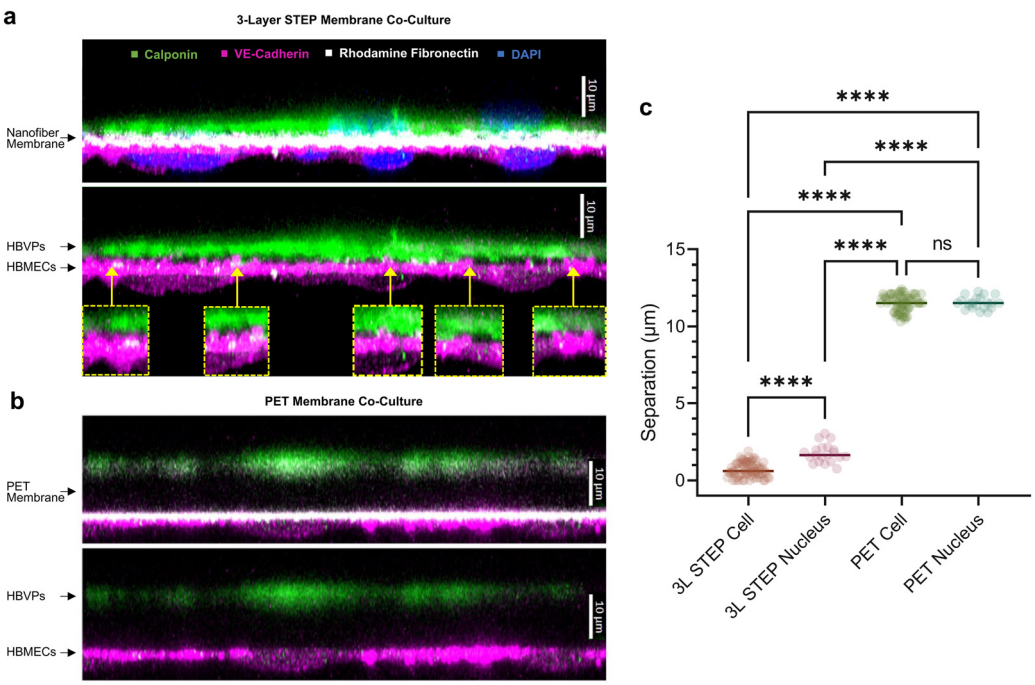

Fig. 4 Nanofiber co-cultures of endothelial cells with pericytes enable cell–cell interactions across the membranes. a) *Z*-Stack images of co-cultures taken with a 63× water lens demonstrate the close-contact of pericytes (green, calponin) and endothelial cells (cyan, VE-cadherin) across the nanofiber membranes. In multiple instances, the endothelial cells and pericytes are reaching into the free space within the membrane (yellow-dashed boxes). b) PET track-etched membranes show significant separation between pericytes (top) and endothelial cells (bottom) which prevents cell–cell interaction. Notice that the imaging quality on the upper side of the PET membrane is significantly reduced due to the mismatch in refractive index of the plastic. In contrast, there is minimal loss of resolution across the nanofiber membranes. c) Measured separation between the stained cellular membranes and nuclei for the nanofiber membrane and the PET membrane. The effective separation between cells (0.68 μm) is significantly smaller than the nominal thickness of the membrane (3 μm) as the cell can reach into the free space within the membrane. Rhodamine-fibronectin on the membranes is white and the DAPI is blue (****$p < 0.0001$).

through the nanofiber membrane. This is not seen for the track-etched membrane in Movie S4,† where there is large separation between the cell monolayers and a loss of resolution for the pericytes on the top of the membrane.

TEER measurements indicate a biological benefit of the ultra-thin and ultra-porous nanofiber co-culture

BBB integrity is commonly assessed by TEER measurements.[66,67] Endothelial monolayers resist electrical current by restricting free ion transport with tight-junction formation. Thus, by applying a small potential across the monolayer and sensing the corresponding electrical current, the resistance of the monolayer can be deduced. Since PET membranes are thick with minimal porosity, pericytes have not been shown to increase TEER measurements as meaningfully as either astrocytes or neurons.[68] This is in part because astrocytes and neurons upregulate tight junctions through soluble factors, while pericytes upregulate tight junctions through peg-and-socket junctions. Soluble factors can pass through the small pores in the thick track-etched membranes, while cells cannot fully reach across for physical contact.

Since our membranes are ultra-thin and ultra-porous, we sought to explore the impact that pericytes may have on tight junction formation. The membranes on conventional 24-well plate transwell inserts were removed and replaced with scaffolds holding our custom nanofiber membranes. HBMECs were cultured on the basolateral side of the membrane, and if co-culture was desired, HBVPs were grown on the apical side. We used stick electrodes to measure the resistance across the membrane. TEER measurements were taken prior to seeding the cells (control) and every day after for 5 consecutive days. The TEER measurements were normalized by the control values to find the contribution of the endothelial cells. The nanofiber membranes had initial resistance values ~3× lower than the PET membranes; however, their nominal TEER increase was equal to or higher than with the PET membrane (Fig. 5a). We observed TEER values for the HBMEC monolayers are within the range previously characterized (20–100 Ω cm^2).[69] The TEER values were equal between monocultures of HBMECs on nanofibers and PET membranes. Since nanofibers had a much lower initial resistance, the percent increase in TEER is significantly larger (Fig. 5b). Next, we looked at the contributions that HBVPs may have on HBMECs tight junction formation. We saw that the co-culture of HBMECs and HBVPs on the PET membrane was not different than either monolayer condition. The nanofiber co-culture, however, had a significant increase in TEER values over both monoculture conditions and the PET co-culture conditions. This indicates that the nanofiber BM more accurately replicates the physiology of the BBB than conventional track-etched membranes.

Discussion

Here we have shown that precisely aligned nanofiber networks can be used to create physiologically relevant basement-membrane mimics. Nanofiber network properties, such as fiber spacing, fiber diameter, fiber orientation, and number of fiber layers can be precisely controlled to create membranes with variable thicknesses and porosities. To our knowledge, our nanofiber membranes significantly exceed the highest reported porosities for membranes used in barrier modeling. At almost 90% porosity, these membranes are near the limit of what might be experimentally possible, and higher porosity membranes are not likely to significantly increase transport across the membranes. While the described 1-layer and 3-layer nanofiber membranes form BM mimics with enhanced

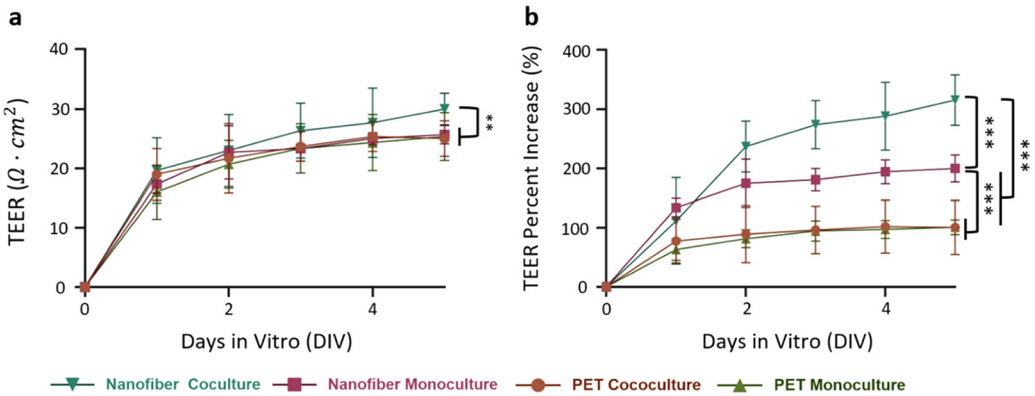

Fig. 5 TEER measurements of HBMEC and HBMEC-HBVP co-cultures indicate a benefit of using STEP nanofiber membranes. Custom transwell inserts were fabricated to generate either a monolayer of endothelial cells (HBMECs) or a co-culture of endothelial cells (HBMECs) and pericytes (HBVPs). a) TEER measurements with stick electrodes on HBMEC monolayers indicate equal TEER values between the 3-layer STEP nanofiber and PET membranes. Co-cultures on the PET membranes had a negligible rise in TEER compared to the monoculture, while the nanofiber membrane co-cultures had a significant increase in TEER values from the monoculture condition (p-value < 0.01). b) The 3-layer nanofiber membranes had a more significant percent increase from base measurements than PET membranes for both monoculture (p-value < 0.001) and coculture conditions (p-value < 0.001). Each data point is given as mean ± std. with $n \geq 3$ (**$p < 0.01$, ***$p < 0.001$).

properties, it may be possible to further optimize these membrane properties by exploring additional fiber diameters, especially smaller diameter fibers. Nanofibers as small as 100 nm in diameter can easily be fabricated with the STEP method. Incorporating smaller diameter fibers could theoretically produce membranes less than 200 nm, reaching the upper end of the *in vivo* brain BM thicknesses. Further, thinner fibers would decrease the surface area for focal adhesion formation, allowing cell–cell contact to dominate compared to cell-surface contact. Fabricating membranes with thinner fibers, however, may compromise membrane strength. Our previous study with a single crosshatch STEP membrane demonstrated a bending stiffness of 0.45 N m^{-1} and an elastic modulus of 150.6 kPa.[63] Our observed elastic modulus is lower than those observed for other fibrous membranes[70] and relative to the lower end of measurements for the *in vivo* basement membrane.[71] Future studies should be conducted to tune the STEP membranes elastic modulus through manipulating fiber layer numbers and thicknesses to achieve a desired value.

Recent work has been performed to create thin fibrous membranes using electrospun poly(ε-caprolactone)[57] membranes coated with collagen. However, due to the electrospinning process, the fibers are not precisely aligned, leading to variability in pore size and local thicknesses. STEP nanofiber membranes overcome this challenge due to the precise control over fiber diameters, spacings, and orientations across multilayered structures. This is demonstrated with a smaller skew in the measured pore sizes than other fibrous membranes,[54–57,66] with <1 μm^2 difference between the median and mean pore size. Consistent generation of intended pore sizes is paramount for applications in transmembrane migration and transport.

Non-fibrous membranes are also popular for BM modelling. Poly(lactide-*co*-caprolactone) membranes have a nominal thickness of 0.95 μm, due to the spin coating method.[72] However, their calculated porosity was between 35 and 40%, significantly lower than our membrane.

We found for the STEP membrane that most nuclei were separated by less distance (1.75 ± 0.60 μm, range 0.75–3 μm) than the nominal membrane thickness, suggesting the cells partially sit within the membrane. This has been observed previously for STEP membranes, where the nucleus shape will remodel around the nanofiber membranes.[64] Jana *et al.* observed that the size and curvature of the nanofibers affects the invagination by the cell and modeling of the nucleus. Briefly, cells sense the interfiber spacing and wrap around and align along the fiber axis, form varying shapes.[63,73] These findings have been validated to match various *in vivo* bahaviors.[74–76]

We integrated our nanofiber membrane into a PDMS microfluidic model; however, absorption and adsorption of molecules by PDMS makes it unfavorable for drug transport studies.[77] Since our nanofibers are polystyrene, an entirely plastic device could be designed and assembled for commercial use. Furthermore, our nanofibers can be integrated into conventional transwell plates, enabling use with current well plate-based equipment to enable rapid adoption. As a proof-of-concept, we modified a conventional 24-transwell plastic insert to integrate the nanofiber scaffold and used them for collecting TEER measurements with stick electrodes.

We cultured endothelial monolayers on the nanofiber scaffolds and demonstrated that the monolayers express key junctional proteins such as ZO-1 and VE-cadherin. Confocal imaging shows that endothelial cells were constrained to only one side of the nanofiber membrane. Furthermore, we were able to co-culture pericytes on the opposite side of the membrane and show that our highly porous and thin membrane enables close contact between endothelial cells and pericytes. From confocal images, it appears that the two monolayers can reach into the membrane to come into direct contact. The benefit of having pericytes in close proximity is supported by the significantly higher TEER measurements of HBMEC and HBVP co-cultures on the nanofibers which suggests that this membrane has advantages over other membranes when replicating *in vivo* physiology. Due to the high porosity of the STEP membrane, the initial resistance values measured were 3–5× lower than for the PET membrane. This resulted in a higher percent increase for TEER measured using the STEP nanofiber membranes. The significantly higher TEER values indicate tighter barrier formation, while the percent increase in TEER measurements suggests that barriers formed on STEP membranes may be more sensitive to changes in TEER values. This would have a benefit in pharmaceutical testing as it allows for more resolution in measuring effects.

Previous studies have shown that migratory astrocytes that cross track-etched membranes for pores as small as 3 μm in diameter.[38] Migratory pericytes or astrocytes across the membrane clearly are not consistent with the *in vivo* configuration but are more realistic for our thin membranes. Our nanofiber networks have significant advantages for studying cell and nanoparticle migration across the BBB. The controllable pore size and high porosity may allow for small cell and nanoparticle migration while keeping large cells to their respective sides of the membrane. Conventional track-etched membranes are unsuitable for nanoparticle transport studies due to the adhesion of nanoparticles to the membranes and within track-etched pores.[43] Our highly porous membrane should minimize interference of the membrane to nanoparticle transport. Likewise, modeling cancer metastasis and immune cell migration across the BBB is of significant importance,[78] and our models should enable high-levels of migration. The larger pore sizes (generally ≥3 μm pores) used for cellular transmigration studies have the disadvantage of allowing endothelial cells to cross the membrane and form a second monolayer on the opposite side of the membrane.[34,38]

Conclusions

Using our suspended nanofiber networks, we achieved high porosity (88%) in ultra-thin fibrous (<3 μm nominal) BM mimics compared with reported literature or commercially

available. Our approach achieved low separation between the cell membrane and nuclei (0.69 μm and 1.75 μm, respectively), thus providing unrestrained opportunity for the cells on either side to contact each other without permitting migration, as would be expected *in vivo*. We expect future studies to further optimize the physical membrane properties and investigate the utility of these networks. We anticipate that our nanofiber networks will improve barrier modeling with implications for drug discovery, cell migration, and disease studies.

Data availability and supplemental

The data that supports the findings of this study are available within the article and its ESI.† See ESI† for additional device images of endothelial cells forming monolayers and co-cultures with pericytes. Movies of *Z*-stack images are also provided to demonstrate the isolation of monolayers while being in close proximity for monoculture and co-culture conditions on nanofiber and PET membranes.

Author contributions

Conceptualization: PMG, EJJ, AJ, RVD, ASN. Methodology: PMG, EJJ, AJ, AA. Materials: AJ, AA Formal analysis: PMG, EJJ. Data curation: PMG, EJJ. Resources: ASN, RVD. Supervision: ASN, RVD.

Conflicts of interest

The authors have pending patents and current patents on the work presented within the manuscript.

Acknowledgements

This research was funded in part by the NIH PO1 (PO1CA207206) and NCATS/NIH (2R44TR003968-02) and completed through the collaboration between the BEMS lab and STEP lab at Virginia Tech. The authors thank Barath Udayasuryan for guidance during this study. P. M. G. is a trainee in the BIOTRANS IGEP program at Virginia Tech and the ICTAS Center for Engineered Health. A. S. N. acknowledges support from the National Science Foundation (grants 1762634, 2119949, and 2107332). The opinions, findings, and conclusions, or recommendations expressed are those of the author(s) and do not necessarily reflect the views of the National Science Foundation. A. S. N. acknowledges support from members of the Spinneret-based Tunable Engineered Parameters (STEP) Lab, Virginia Tech, and thanks the Institute of Critical Technologies and Sciences (ICTAS) and Macromolecules Innovation Institute at Virginia Tech for the support to conduct this study.

References

1 C. M. Sakolish, M. B. Esch, J. J. Hickman, M. L. Shuler and G. J. Mahler, Modeling barrier tissues in vitro: methods, achievements, and challenges, *EBioMedicine*, 2016, **5**, 30–39.
2 D. Huh, *et al.* Reconstituting organ-level lung functions on a chip, *Science*, 2010, **328**, 1662–1668.
3 J. Shrestha, *et al.* Lung-on-a-chip: the future of respiratory disease models and pharmacological studies, *Crit. Rev. Biotechnol.*, 2020, **40**, 213–230.
4 N. Ashammakhi, *et al.* Gut-on-a-chip: Current progress and future opportunities, *Biomaterials*, 2020, 120196.
5 E. Sutterby, P. Thurgood, S. Baratchi, K. Khoshmanesh and E. Pirogova, Microfluidic Skin-on-a-Chip Models: Toward Biomimetic Artificial Skin, *Small*, 2020, **16**, 2002515.
6 M. J. Wilmer, *et al.* Kidney-on-a-chip technology for drug-induced nephrotoxicity screening, *Trends Biotechnol.*, 2016, **34**, 156–170.
7 H. C. Helms, *et al.* In vitro models of the blood–brain barrier: an overview of commonly used brain endothelial cell culture models and guidelines for their use, *J. Cereb. Blood Flow Metab.*, 2016, **36**, 862–890.
8 L. Jiang, S. Li, J. Zheng, Y. Li and H. Huang, Recent progress in microfluidic models of the blood-brain barrier, *Micromachines*, 2019, **10**, 375.
9 M. E. Katt and E. V. Shusta, In vitro models of the blood-brain barrier: building in physiological complexity, *Curr. Opin. Chem. Eng.*, 2020, **30**, 42–52.
10 S. Musafargani, *et al.* Blood brain barrier: A tissue engineered microfluidic chip, *J. Neurosci. Methods*, 2020, **331**, 108525.
11 A. Oddo, *et al.* Advances in microfluidic blood–brain barrier (BBB) models, *Trends Biotechnol.*, 2019, **37**, 1295–1314.
12 A. Prashanth, *et al.* Are In Vitro Human Blood–Brain–Tumor-Barriers Suitable Replacements for In Vivo Models of Brain Permeability for Novel Therapeutics?, *Cancers*, 2021, **13**, 955.
13 M. W. van Der Helm, A. D. Van Der Meer, J. C. Eijkel, A. van den Berg and L. I. Segerink, Microfluidic organ-on-chip technology for blood-brain barrier research, *Tissue Barriers*, 2016, **4**, e1142493.
14 Z. Cai, *et al.* Role of blood-brain barrier in Alzheimer's disease, *J. Alzheimer's Dis.*, 2018, **63**, 1223–1234.
15 D. Huh, *et al.* A human disease model of drug toxicity–induced pulmonary edema in a lung-on-a-chip microdevice, *Sci. Transl. Med.*, 2012, **4**, 159ra147.
16 A. C. Webster, E. V. Nagler, R. L. Morton and P. Masson, Chronic kidney disease, *Lancet*, 2017, **389**, 1238–1252.
17 B. E. Kim and D. Y. Leung, Significance of skin barrier dysfunction in atopic dermatitis, *Allergy, Asthma Immunol. Res.*, 2018, **10**, 207.
18 W. M. Pardridge, Blood–brain barrier delivery, *Drug Discovery Today*, 2007, **12**, 54–61.
19 F. Sivandzade and L. Cucullo, In-vitro blood–brain barrier modeling: A review of modern and fast-advancing technologies, *J. Cereb. Blood Flow Metab.*, 2018, **38**, 1667–1681, DOI: **10.1177/0271678x18788769**.
20 L. Xu, A. Nirwane and Y. Yao, Basement membrane and blood–brain barrier, *Stroke Vasc. Neurol.*, 2019, **4**, 78–82.
21 D. L. Viana, D. J. Alladagbin, W. L. C. Dos-Santos and C. P. Figueira, A comparative study of human glomerular basement membrane thickness using direct measurement

and orthogonal intercept methods, *BMC Nephrol.*, 2022, **23**, 23, DOI: 10.1186/s12882-021-02634-1.
22 E. A. Winkler, R. D. Bell and B. V. Zlokovic, Central nervous system pericytes in health and disease, *Nat. Neurosci.*, 2011, **14**, 1398.
23 N. J. Abbott, Astrocyte-endothelial interactions and blood-brain barrier permeability*, *J. Anat.*, 2002, **200**, 629–638, DOI: 10.1046/j.1469-7580.2002.00064.x.
24 N. J. Abbott, Blood–brain barrier structure and function and the challenges for CNS drug delivery, *J. Neurosci. Methods*, 2013, **36**, 437–449, DOI: 10.1007/s10545-013-9608-0.
25 B. P. Daniels, *et al.* Immortalized human cerebral microvascular endothelial cells maintain the properties of primary cells in an in vitro model of immune migration across the blood brain barrier, *J. Neurosci. Methods*, 2013, **212**, 173–179, DOI: 10.1016/j.jneumeth.2012.10.001.
26 H. H. Chung, M. Mireles, B. J. Kwarta and T. R. Gaborski, Use of porous membranes in tissue barrier and co-culture models, *Lab Chip*, 2018, **18**, 1671–1689.
27 J. Banerjee, Y. Shi and H. S. Azevedo, In vitro blood–brain barrier models for drug research: state-of-the-art and new perspectives on reconstituting these models on artificial basement membrane platforms, *Drug Discovery Today*, 2016, **21**, 1367–1386.
28 M. Bonakdar, P. M. Graybill and R. V. Davalos, A microfluidic model of the blood-brain barrier to study permeabilization by pulsed electric fields, *RSC Adv.*, 2017, **7**, 42811–42818, DOI: 10.1039/C7RA07603G.
29 N. J. Douville, *et al.* Fabrication of two-layered channel system with embedded electrodes to measure resistance across epithelial and endothelial barriers, *Anal. Chem.*, 2010, **82**, 2505–2511.
30 E. M. Frohlich, *et al.* Topographically-patterned porous membranes in a microfluidic device as an in vitro model of renal reabsorptive barriers, *Lab Chip*, 2013, **13**, 2311–2319.
31 S. Hosic, *et al.* Rapid prototyping of multilayer microphysiological systems, *ACS Biomater. Sci. Eng.*, 2020, **7**(7), 2963, DOI: 10.1021/acsbiomaterials.0c00190.
32 S. Jeong, *et al.* A three-dimensional arrayed microfluidic blood–brain barrier model with integrated electrical sensor array, *IEEE Trans. Biomed. Eng.*, 2017, **65**, 431–439.
33 G. S. Ugolini, *et al.* Design and validation of a microfluidic device for blood–brain barrier monitoring and transport studies, *J. Micromech. Microeng.*, 2018, **28**, 044001.
34 E. Vandenhaute, *et al.* Adapting coculture in vitro models of the blood–brain barrier for use in cancer research: maintaining an appropriate endothelial monolayer for the assessment of transendothelial migration, *Lab. Invest.*, 2016, **96**, 588–598.
35 F. R. Walter, *et al.* A versatile lab-on-a-chip tool for modeling biological barriers, *Sens. Actuators, B*, 2016, **222**, 1209–1219.
36 J. D. Wang, E.-S. Khafagy, K. Khanafer, S. Takayama and M. E. ElSayed, Organization of endothelial cells, pericytes, and astrocytes into a 3D microfluidic in vitro model of the blood–brain Barrier, *Mol. Pharmaceutics*, 2016, **13**, 895–906.
37 Y. I. Wang, H. E. Abaci and M. L. Shuler, Microfluidic blood–brain barrier model provides in vivo-like barrier properties for drug permeability screening, *Biotechnol. Bioeng.*, 2017, **114**, 184–194.
38 D. M. Wuest, A. M. Wing and K. H. Lee, Membrane configuration optimization for a murine in vitro blood–brain barrier model, *J. Neurosci. Methods*, 2013, **212**, 211–221.
39 R. Booth and H. Kim, Characterization of a microfluidic in vitro model of the blood-brain barrier (μBBB), *Lab Chip*, 2012, **12**, 1784–1792, DOI: 10.1039/C2LC40094D.
40 S. H. Ma, L. A. Lepak, R. J. Hussain, W. Shain and M. L. Shuler, An endothelial and astrocyte co-culture model of the blood–brain barrier utilizing an ultra-thin, nanofabricated silicon nitride membrane, *Lab Chip*, 2005, **5**, 74–85.
41 A. Mossu, *et al.* A silicon nanomembrane platform for the visualization of immune cell trafficking across the human blood–brain barrier under flow, *J. Cereb. Blood Flow Metab.*, 2019, **39**, 395–410.
42 A. T. Salminen, *et al.* Ultrathin Dual-Scale Nano-and Microporous Membranes for Vascular Transmigration Models, *Small*, 2019, **15**, 1804111.
43 E. De Jong, D. S. Williams, L. K. Abdelmohsen, J. C. Van Hest and I. S. Zuhorn, A filter-free blood-brain barrier model to quantitatively study transendothelial delivery of nanoparticles by fluorescence spectroscopy, *J. Controlled Release*, 2018, **289**, 14–22.
44 W. McIntosh Ambrose, *et al.* Collagen Vitrigel membranes for the in vitro reconstruction of separate corneal epithelial, stromal, and endothelial cell layers, *J. Biomed. Mater. Res., Part B*, 2009, **90**, 818–831.
45 T. Takezawa, K. Ozaki, A. Nitani, C. Takabayashi and T. Shimo-Oka, Collagen vitrigel: a novel scaffold that can facilitate a three-dimensional culture for reconstructing organoids, *Cell Transplant.*, 2004, **13**, 463–474.
46 A. Shima, S. Nagata and S. Takeuchi, Three-dimensional co-culture of blood-brain barrier-composing cells in a culture insert with a collagen vitrigel membrane, *In Vitro Cell. Dev. Biol.*, 2020, 1–5.
47 T. Takezawa, *et al.* Collagen vitrigel membrane useful for paracrine assays in vitro and drug delivery systems in vivo, *J. Biotechnol.*, 2007, **131**, 76–83.
48 M. J. Mondrinos, Y.-S. Yi, N.-K. Wu, X. Ding and D. Huh, Native extracellular matrix-derived semipermeable, optically transparent, and inexpensive membrane inserts for microfluidic cell culture, *Lab Chip*, 2017, **17**, 3146–3158.
49 W. Quirós-Solano, *et al.* Microfabricated tuneable and transferable porous PDMS membranes for Organs-on-Chips, *Sci. Rep.*, 2018, **8**, 1–11.
50 A. Sabirova, F. Pisig, N. Rayapuram, H. Hirt and S. P. Nunes, Nanofabrication of isoporous membranes for cell fractionation, *Sci. Rep.*, 2020, **10**, 1–9.
51 M. Zakharova, *et al.* Multiplexed blood–brain barrier organ-on-chip, *Lab Chip*, 2020, **20**, 3132–3143.
52 J. D. Patient, *et al.* Nanofibrous scaffolds support a 3D in vitro permeability model of the human intestinal epithelium, *Front. Pharmacol.*, 2019, **10**, 456, DOI: 10.3389/fphar.2019.00456.

53 M. Zakharova, *et al.* Transwell-Integrated 2 μm Thick Transparent Polydimethylsiloxane Membranes with Controlled Pore Sizes and Distribution to Model the Blood-Brain Barrier, *Adv. Mater. Technol.*, 2021, **6**(12), DOI: **10.1002/admt.202100138**.

54 P. Y. Dankers, *et al.* Bioengineering of living renal membranes consisting of hierarchical, bioactive supramolecular meshes and human tubular cells, *Biomaterials*, 2011, **32**, 723–733.

55 S. Eom, S. M. Park, S. J. Han, J. W. Kim and D. S. Kim, One-step fabrication of a tunable nanofibrous well insert via electrolyte-assisted electrospinning, *RSC Adv.*, 2017, **7**, 38300–38306.

56 J. H. Kim, *et al.* A Microfluidic Chip Embracing a Nanofiber Scaffold for 3D Cell Culture and Real-Time Monitoring, *Nanomaterials*, 2019, **9**, 588.

57 D. Kim, S. Eom, S. M. Park, H. Hong and D. S. Kim, A collagen gel-coated, aligned nanofiber membrane for enhanced endothelial barrier function, *Sci. Rep.*, 2019, **9**, 14915, DOI: **10.1038/s41598-019-51560-8**.

58 C.-M. Lo, C. R. Keese and I. Giaever, Cell–substrate contact: another factor may influence transepithelial electrical resistance of cell layers cultured on permeable filters, *Exp. Cell Res.*, 1999, **250**, 576–580.

59 A. Ogaki, T. Araki, M. Ishikawa, Y. Ikegaya and R. Koyama, A live imaging-friendly slice culture method using collagen membranes, *Neuropsychopharmacol. Rep.*, 2020, **40**, 307–313.

60 A. S. Nain and J. Wang, Polymeric nanofibers: isodiametric design space and methodology for depositing aligned nanofiber arrays in single and multiple layers, *Polym. J.*, 2013, **45**, 695–700, DOI: **10.1038/pj.2013.1**.

61 J. Wang and A. S. Nain, Suspended micro/nanofiber hierarchical biological scaffolds fabricated using non-electrospinning STEP technique, *Langmuir*, 2014, **30**, 13641–13649, DOI: **10.1021/la503011u**.

62 J. Zeltinger, J. Sherwood, D. Graham, R. Mueller and L. Griffith, Effect of Pore Size and Void Fraction on Cellular Adhesion, Proliferation, and Matrix Deposition, *Tissue Eng.*, 2001, **7**, 557.

63 A. Jana, *et al.* Crosshatch nanofiber networks of tunable interfiber spacing induce plasticity in cell migration and cytoskeletal response, *FASEB J.*, 2019, **33**, 10618–10632, DOI: **10.1096/fj.201900131R**.

64 A. Jana, *et al.* Sculpting Rupture-Free Nuclear Shapes in Fibrous Environments, *Adv. Sci.*, 2022, e2203011, DOI: **10.1002/advs.202203011**.

65 C. R. Justus, N. Leffler, M. Ruiz-Echevarria and L. V. Yang, Cell Migration and Invasion Assays, *J. Visualized Exp.*, 2014, **88**, 51046, DOI: **10.3791/51046**.

66 K. Benson, S. Cramer and H.-J. Galla, Impedance-based cell monitoring: barrier properties and beyond, *Fluids Barriers CNS*, 2013, **10**, 1–11.

67 M. W. van der Helm, *et al.* Direct quantification of transendothelial electrical resistance in organs-on-chips, *Biosens. Bioelectron.*, 2016, **85**, 924–929.

68 A. Appelt-Menzel, *et al.* Establishment of a Human Blood-Brain Barrier Co-culture Model Mimicking the Neurovascular Unit Using Induced Pluri- and Multipotent Stem Cells, *Stem Cell Rep.*, 2017, **8**, 894–906, DOI: **10.1016/j.stemcr.2017.02.021**.

69 A. Paradis, D. Leblanc and N. Dumais, Optimization of an in vitro human blood-brain barrier model: Application to blood monocyte transmigration assays, *MethodsX*, 2016, **3**, 25–34, DOI: **10.1016/j.mex.2015.11.009**.

70 J. W. Choi, J. Youn, D. S. Kim and T. E. Park, Human iPS-derived blood-brain barrier model exhibiting enhanced barrier properties empowered by engineered basement membrane, *Biomaterials*, 2023, **293**, 121983, DOI: **10.1016/j.biomaterials.2022.121983**.

71 S. van Helvert, C. Storm and P. Friedl, Mechanoreciprocity in cell migration, *Nat. Cell Biol.*, 2018, **20**, 8–20, DOI: **10.1038/s41556-017-0012-0**.

72 J. Yoo, *et al.* Use of Elastic, Porous, and Ultrathin Co-Culture Membranes to Control the Endothelial Barrier Function via Cell Alignment, *Adv. Funct. Mater.*, 2020, **31**(9), DOI: **10.1002/adfm.202008172**.

73 E. J. Jacobs Iv, *et al.*, Engineering high post-electroporation viabilities and transfection efficiencies for elongated cells on suspended nanofiber networks, *Bioelectrochemistry*, 2023, **152**, 108415, DOI: **10.1016/j.bioelechem.2023.108415**.

74 J. Singh, A. Pagulayan, B. A. Camley and A. S. Nain, Rules of contact inhibition of locomotion for cells on suspended nanofibers, *Proc. Natl. Acad. Sci. U. S. A.*, 2021, **118**(12), e2011815118, DOI: **10.1073/pnas.2011815118**.

75 R. K. Sadhu, *et al.* Experimental and theoretical model for the origin of coiling of cellular protrusions around fibers, *Nat. Commun.*, 2023, **14**, 5612, DOI: **10.1038/s41467-023-41273-y**.

76 P. Sharma, *et al.* Aligned fibers direct collective cell migration to engineer closing and nonclosing wound gaps, *Mol. Biol. Cell*, 2017, **28**, 2579–2588, DOI: **10.1091/mbc.E17-05-0305**.

77 E. Berthier, E. W. Young and D. Beebe, Engineers are from PDMS-land, Biologists are from Polystyrenia, *Lab Chip*, 2012, **12**, 1224–1237.

78 L. C. Kelley, L. L. Lohmer, E. J. Hagedorn and D. R. Sherwood, Traversing the basement membrane in vivo: a diversity of strategies, *J. Cell Biol.*, 2014, **204**, 291–302.

